Large Eddy Simulation of Supersonic Jet Flow Using Low Order Spatial Discretization Schemes

Carlos Junqueira-Junior, junior.hmg@gmail.com[1]
Sami Yamouni, sami.yamouni@gmail.com[2]
João Luiz F. Azevedo, joaoluiz.azevedo@gmail.com[1]
William R. Wolf, wolf@fem.unicamp.br[1]

[1]Instituto de Aeronáutica e Espaço
[2]Instituto Tecnológico de Aeronáutica
[3]Universidade Estadual de Campinas

Abstract: *The present work presents a compact study of the effects of the use of 2nd-order spatial discretization for unsteady compressible jet flows. The large eddy simulation formulation is written using the finite difference approach, with an explicit time integration and using a second order spatial discretization. The energy equation is carefully discretized in order to model the energy equation of the filtered Navier-Stokes formulation. The classical Smagorinsky model, the dynamic Smagorinsky model and the Vreman model are the chosen subgrid scale closures for the present work. Numerical simulations of perfectly expanded jets are performed and compared with the literature in order to validate and compare the performance of each subgrid closure in the solver.*
Keywords: *Large Eddy Simulations, Compressible Jet Flows, Subgrid Scale models*

1. INTRODUCTION

The large eddy simulation of turbulent incompressible flows is a powerfull tool commonly applied by the scientific community and already introduced in the industry. However, the large eddy simulation of turbulent compressible flows is relatively new. There are still some concepts that are not accurately defined and they challenge the present work. There are discussions in the LES community about the real effects of SGS models. There are important work reporting significant effort to model subgrid tensors for compressible LES (Lilly, 1965; Smagorinsky, 1963; Speziale *et al.*, 1988; Germano *et al.*, 1991; Moin *et al.*, 1991). Compared to the incompressible formulation, new subgrid terms of the energy equation need to be correctly treated in order to achieve results that represent the physics of the simulated problem. On the other hand, there are other studies questioning the physical effects included in algebraic models. 1-D numerical studies of the equation of Burgers using high order methods for spatial discratization, have indicated that large eddy simulations without subgrid scale modeling can, in some cases, reproduce better results when compared with LES using SGS modeling (Li and Wang, 2015).

Another open issue is related to the numerical discretization. There are very important publications on compressible large eddy simulation using high order discretization schemes (Bodony and Lele, 2005, 2008; Bogey and Bailly, 2005; Bogey *et al.*, 2012; Lele, 1992; Lele *et al.*, 2010; Wolf and Lele, 2011). The literature claims LES need sofisticated numerical schemes in order to avoid non physical dissipation in the results. However, some recent work have achieved good results using centered spatial discretization with 2nd order of precision (Mahesh *et al.*, 2004; Mendez *et al.*, 2010, 2012; Brès *et al.*, 2012). The present work focuses on the effects of subgrid scale modeling on low order discretizations for compressible large eddy simulations. Numerical simulations of a perfectly expanded jet are performed using different mesh configurations and different SGS closures. Results are compared with numerical (Mendez *et al.*, 2010) and experimental (Bridges and Wernet, 2008) data.

The LES formulation is written using the finite difference approach. Inviscid numerical fluxes are calculated using a second order accurate centered scheme with the explicit addition of artificial dissipation. A five steps second order accurate Runge-Kutta is the chosen time marching method. A formulation based on the System I set of equations (Vreman, 1995) is used here in order to model the filtered terms of the energy equation. The classical Smagorinsky model (Smagorinsky, 1963; Lilly, 1965, 1967), the dynamic Smagorinsky model (Germano *et al.*, 1991; Moin *et al.*, 1991) and the Vreman model (Vreman, 2004) are the subgrid scale (SGS) turbulence closures used in the present work.

2. LARGE EDDY SIMULATION FILTERING

The large eddy simulation is based on the principle of scale separation, which is addressed as a filtering procedure in a mathematical formalism. A modified version of the the System I filtering approach (Vreman, 1995) is used in present

work which is given by

$$\begin{gathered}\frac{\partial \overline{\rho}}{\partial t}+\frac{\partial}{\partial x_j}\left(\overline{\rho}\widetilde{u_j}\right)=0\,,\\ \frac{\partial}{\partial t}\left(\overline{\rho}\widetilde{u_i}\right)+\frac{\partial}{\partial x_j}\left(\overline{\rho}\widetilde{u_i}\widetilde{u_j}\right)+\frac{\partial \overline{p}}{\partial x_i}-\frac{\partial \tau_{ij}}{\partial x_j}+\frac{1}{3}\frac{\partial}{\partial x_j}\left(\delta_{ij}\sigma_{ii}\right)=0\,,\\ \frac{\partial \overline{e}}{\partial t}+\frac{\partial}{\partial x_j}\left[\left(\overline{e}+\overline{p}\right)\widetilde{u_j}\right]-\frac{\partial}{\partial x_j}\left(\tau_{ij}\widetilde{u_i}\right)+\frac{1}{3}\frac{\partial}{\partial x_j}\left[\left(\delta_{ij}\sigma_{ii}\right)\widetilde{u_i}\right]+\frac{\partial q_j}{\partial x_j}=0\,,\end{gathered} \tag{1}$$

in which t and x_i are independent variables representing time and spatial coordinates of a Cartesian coordinate system **x**, respectively. The components of the velocity vector **u** are written as u_i, and $i = 1, 2, 3$. Density, pressure and total energy per mass unit are denoted by ρ, p and e, respectively. The $\bar{(\cdot)}$ and $\tilde{(\cdot)}$ operators are used in order to represent filtered and Favre averaged properties, respectively. The System I formulation neglectes the double correlation term and the total energy per mass unit is written as

$$\overline{e}=\frac{\overline{p}}{\gamma-1}+\frac{1}{2}\rho\widetilde{u_i}\widetilde{u_i}\,. \tag{2}$$

The heat flux, q_j, is given by

$$q_j=\left(\kappa+\kappa_{sgs}\right)\frac{\partial \widetilde{T}}{\partial x_j}\,. \tag{3}$$

where T is the static temperature and κ is the thermal conductivity, which can by expressed by

$$\kappa=\frac{\mu C_p}{Pr}\,, \tag{4}$$

The thermal conductivity is a function of the specific heat at constant pressure, Cp, of the Prandtl number, Pr, which is equal to 0.72 for air, and of the dynamic viscosity, μ. The SGS thermal conductivity, κ_{sgs}, is written as

$$\kappa_{sgs}=\frac{\mu_{sgs}C_p}{Pr_{sgs}}\,, \tag{5}$$

where Pr_{sgs} is the SGS Prandtl number, which is equal to 0.9 for static SGS models and μ_{sgs} is the eddy viscosity which is calculated by the SGS closure. The dynamic viscosity, μ can be calculated using the Sutherland Law,

$$\mu\left(\widetilde{T}\right)=\mu_\infty\left(\frac{\widetilde{T}}{\widetilde{T}_\infty}\right)^{\frac{3}{2}}\frac{\widetilde{T}_0+S_1}{\widetilde{T}+S_1}\quad\text{with } S_1=110.4K\,. \tag{6}$$

Density, static pressure and static temperature are correlated by the equation of state given by

$$\overline{p}=\rho R\widetilde{T}\,, \tag{7}$$

where R is the gas constant, written as

$$R=C_p-C_v\,, \tag{8}$$

and C_v is the specif heat at constant volume. The shear-stress tensor, τ_{ij}, is written according to the Stokes hypothesis and includes the eddy viscosity, μ_{sgs},

$$\tau_{ij}=2\left(\mu+\mu_{sgs}\right)\left(\tilde{S}_{ij}-\frac{1}{3}\delta_{ij}\tilde{S}_{kk}\right) \tag{9}$$

in which $\tilde{S}_{ij}$, components of rate-of-strain tensor, are given by

$$\tilde{S}_{ij}=\frac{1}{2}\left(\frac{\partial \tilde{u}_i}{\partial x_j}+\frac{\partial \tilde{u}_j}{\partial x_i}\right)\,. \tag{10}$$

The SGS stress tensor components are written using the eddy viscosity (Sagaut, 2002),

$$\sigma_{ij}=-2\mu_{sgs}\left(\tilde{S}_{ij}-\frac{1}{3}\tilde{S}_{kk}\right)+\frac{1}{3}\delta_{ij}\sigma_{kk}\,. \tag{11}$$

The eddy viscosity, μ_{sgs}, and the components of the isotropic part of the SGS stress tensor, σ_{kk}, are modeled by the SGS closure. The Smagorinsky model (Smagorinsky, 1963), the dynamic Smagorinsky model (Moin *et al.*, 1991) and the Vreman model (Vreman, 2004) are the SGS closures used in the present work. The detailed formulation is presented in the work of Junqueira-Junior (2016).

3. NUMERICAL FORMULATION

The governing equations previously described are re-written in a dimensionless general curvilinear coordinate system fashion. The formulation is discretized in a structured finite difference coordinate system (Bigarella, 2002). The numerical flux is calculated through a central difference scheme with the explicit addition of the anisotropic scalar artificial dissipation of Turkel and Vatsa (1994). The time integration is performed by an explicit, 2nd-order, 5-stage Runge-Kutta scheme (Jameson and Mavriplis, 1986; Jameson *et al.*, 1981). Conserved properties and artificial dissipation terms are properly treated near boundaries in order to assure the physical correctness of the numerical formulation. Details of the numerical approach can be found in the work of Junqueira-Junior *et al.* (2015) and Junqueira-Junior (2016).

4. BOUNDARY CONDITIONS

The geometry used in the present work presents a cylindrical shape which is gererated by the rotation of a 2-D plan around a centerline. Figure 1 presents a lateral view and a frontal view of the computational domain used in the present work and the positioning of the entrance, exit, centerline, far field and periodic boundary conditions. The reader can find the formulation of the boundary condition in the work of Junqueira-Junior *et al.* (2015) and Junqueira-Junior (2016).

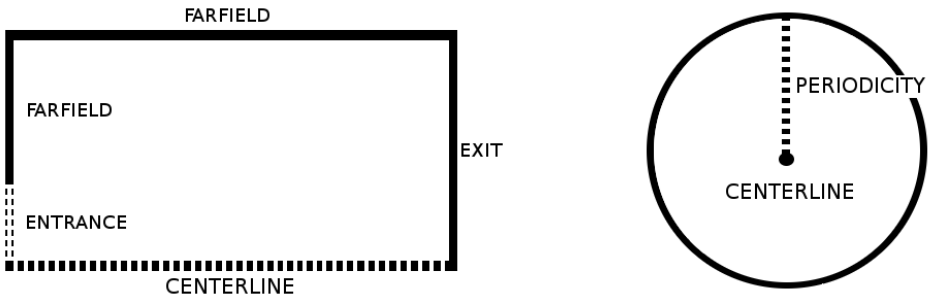

(a) Lateral view of boundary conditions. (b) Frontal view of boundary conditions.

Figura 1: Lateral and frontal views of the computational domain indicating boundary conditions.

5. STUDY OF SUPERSONIC JET FLOW

Four numerical studies are performed in the present research in order to study the use of 2nd-order spatial discretization on large eddy simulations of a perfectly expanded jet flow configuration. The effects of mesh refinement and SGS models are compared in the present work. Two different meshes are created for the refinement study. The three SGS models implemented in the code, classic Smagorinsky, dynamic Smagorinsky and Vreman, are compared in the current section. Results are compared with analytical, numerical and experimental data from the literature (Mendez *et al.*, 2010, 2012; Bridges and Wernet, 2008).

5.1 Mesh Configurations

Two different geometries are created for the simulations discussed in the current work. One geometry presents a cylindrical shape and the other one presents a divergent conical shape. For the sake of simplicity, the round geometry is named geometry A and the other one is named geometry B in present text. One grid is generated for each geometry used in the present study. These computational grids are named mesh A and mesh B. Mesh B is created based on results using mesh A. One illustration of the computational grids is presented in Fig. 2. Mesh A is created using a mesh generator developed by the research group for the cylindrical shape configuration. This computational mesh is composed by 400 points in the axial direction, 200 points in the radial direction and 180 points in the azimuthal direction, which originates 14.4 million grid points. Hyperbolic tangent functions are used for the points distribution in the radial and axial directions. Grid points are clustered near the shear layer of the jet. The mesh is coarsened towards the outer regions of the domain in order to dissipate properties of the flow far from the jet. Such mesh refinement approach can avoid reflection of information into the domain. Mesh A is created based on a reference grid of Mendez *et al.* (2010, 2012).

Mesh B is composed by 343 points in the axial direction, 398 points in the radial direction and 360 points in the azimuthal direction, which yields approximately 50 million grid points. The 2-D mesh is generated with ANSYS® ICEM CFD (ANSYS, 2016). The points are allocated using different distributions in eight edges of the 2-D domain. The same coarsening approach used for mesh A is also applied for mesh B. The distance between mesh points increase towards the outer region of the domain. This procedure force the dissipation of properties far from the jet in order to avoid reflection of data into the domain. The reader can find more details about the mesh generation on the work of Junqueira-Junior (2016).

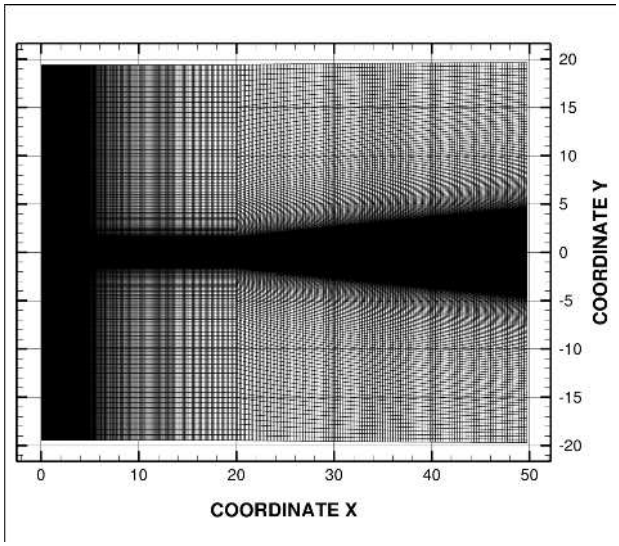

(a) 2-D view of mesh A in the XZ plan.

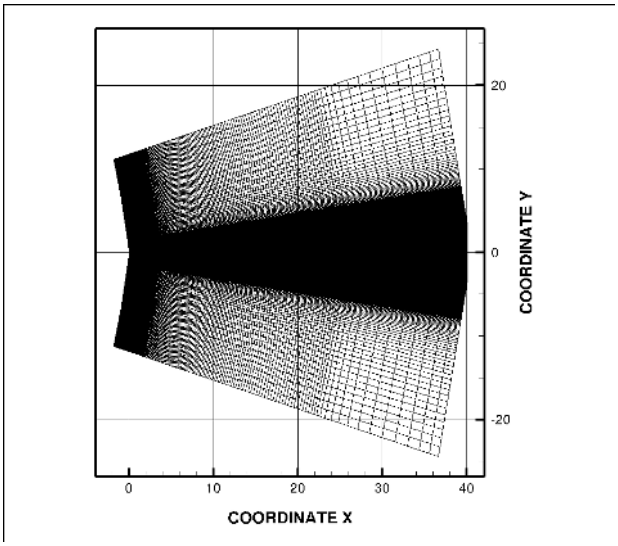

(b) 2-D view of mesh B in the XZ plan.

Figura 2: 2-D view of the computational meshes used in the current work.

5.2 Flow Configuration and Boundary Conditions

An unheated perfectly expanded jet flow is chosen to validate the LES tool. The flow is characterized by an unheated perfectly expanded inlet jet with a Mach number of 1.4 at the domain entrance. Therefore, the pressure ratio, $PR = P_j/P_\infty$, and the temperature ratio, $TR = T_j/T_\infty$, between the jet exit and the ambient freestream conditions, are equal to one, *i.e.*, $PR = 1$ and $TR = 1$. The Reynolds number of the jet is $Re = 1.57 \times 10^6$, based on the jet exit diameter. This flow configuration is chosen due to the absence of strong shocks waves. Strong discontinuities must be carefully treated using numerical approaches which are not yet implemented into the solver. Moreover, numerical and experimental data of this flow configuration are available in the literature such as the work Mendez *et al.* (2010, 2012) and the work of Bridges and Wernet (2008).

The boundary conditions discussed in section 4are used in the simulations performed in the current thesis. Figure 1 presented a lateral view and a frontal view of the computational domain used by the simulation in where the positioning of each boundary condition is indicated. A top-hat velocity profile, with $M = 1.4$, is used at the entrance boundary. Riemann invariants are used at the farfield regions. A special singularity treatment is performed at the centerline. A periodicity is imposed in the azimuthal direction in order to create a transparency for the flow.

Properties of flow at the inlet and at the farfield regions have to be provided to the code in order to impose the boundary conditions. Density, ρ, temperature, T, velocity, U, Reynolds number Re, and specific heat at constant volume, C_v, are provided in the dimensionless form to the simulation. These properties are given by

$$\begin{array}{llll} \rho_j = 1.00\,, & T_j = 1.00\,, & U_j = 1.4\,, & Re_j = 1.57 \times 10^6\,, \\ \rho_\infty = 1.00\,, & T_\infty = 1.00\,, & U_\infty = 0.00\,, & C_v = 1.786\,, \end{array} \tag{12}$$

where the j subscript stands for property at the jet entrance and the ∞ subscript stands for property at the farfield region.

5.3 Large Eddy Simulations

Four simulations are performed in the present draft. The objective is to study the effects of mesh refinement and to evaluate the three different SGS models included into the code. The calculations are performed in two steps. First a preliminary simulation is performed in order to achieve a statistically steady state condition. In the sequence, the simulations are run for another period in order to collect enough data for the calculation of time averaged properties of the flow and its fluctuations.

The configurations of all simulations are discussed in the current section, towards the description of the preliminary calculations which are performed in order to drive the flow to a statistically steady flow condition. Table 1 presents the operating conditions of all four numerical studies performed in the current research. Mesh A is only used on S1. The other calculations are performed using the refined grid, Mesh B. The stagnated flow condition is used as initial condition for all simulations but S3, which uses the solution of S2 after 10.15 flow through times (FTT). One flow through time is the necessary time for a particle to cross all the domain considering the inlet velocity of the jet. The dimensionless time increment used for all configurations is the biggest one which the solver can handle without diverging the solution. The static Smagorinsky model (Smagorinsky, 1963; Lilly, 1965, 1967) is used on S1 and S2. The dynamic Smagorinsky model (Germano *et al.*, 1991; Moin *et al.*, 1991) and the Vreman model (Vreman, 2004) are used on S3 and S4, respectively.

The last column of Tab. 1 represents the period simulated by all numerical studies in order to achieve the statistically steady state flow condition. Moreover, the table provides informations about time increment and inital conditions.

Tabela 1: Configuration of large eddy simulations performed in the present work

Simulation	Mesh	SGS	Δt	Initial condition	FTT
S1	A	Static Smagorinsky	2.5×10^{-5}	Stagnated flow	37.8
S2	B	Static Smagorinsky	1×10^{-4}	Stagnated flow	10.15
S3	B	Dynamic Smagorinsky	5×10^{-5}	Stagnated flow	5.86
S4	B	Vreman	1×10^{-4}	S2 – 10.15 FTT	13.65

The simulations are restarted and run for another period in which data of the flow are extracted and recorded in a fixed frequency after the preliminary study. The collected data are time averaged in order to calculate mean properties of the flow and compare with the results of the numerical and experimental references.

In the present work, time averaged properties are notated as $\langle \cdot \rangle$. Table 2 presents the configuration of simulations performed in order to calculate mean flow properties. The second column presents the number of extractions performed during the simulations. Data are extracted each 0.02 dimensionless time in the present work which is equivalent to a dimensionless frequency of 50. The choice of this frequency is based on the numerical work reported in the work of Mendez *et al.* (2010, 2012). The last two columns of Tab. 2 present the total dimensionless time simulated to calculate the mean properties.

Tabela 2: Time average configuration

Simulation	Nb. Extractions	Frequency	Total time
S1	2048	50	40.96 (1.14 FTT)
S2	3365	50	67.3 (2.36 FTT)
S3	2841	50	56.6 (1.98 FTT)
S4	1543	50	30.86 (1.08 FTT)

5.4 Study of Mesh Refinement Effects

Effects of mesh refinement on compressible LES are discussed in the present section. Profiles of properties calculated by S1 and S2 simulations are collected and compared with numerical and experimental results from the literature (Mendez *et al.*, 2010, 2012; Bridges and Wernet, 2008). Both simulations use the same SGS model, the static Smagorinsky model (Smagorinsky, 1963; Lilly, 1965, 1967). Mesh A is used on S1 simulation and Mesh B is used on S2 calculation. Figure 3 illustrates the positioning of surfaces and profiles extracted for all simulations performed in the current work.

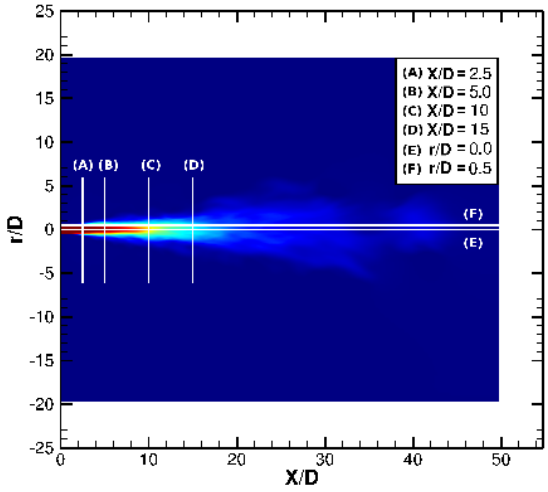

Figura 3: Positioning in the computational domain of surfaces studied in the present work

One important characteristic of a round jet flow configurations is the potential core length, $\delta_j^{95\%}$. The potential core, $U_j^{95\%}$, is defined as 95% of the velocity of the jet at the inlet. Therefore, the potential core length can be defined as the positioning in the centerline where $U_j^{95\%}$ is located. Time averaged results of the axial component of velocity are presented in the subsection. Table 3 presents the size of the potential core of S1, S2 computations and the numerical results from the work of Mendez *et al.* (2010, 2012), along with the relative error compared with the experimental data of Bridges and Wernet (2008).

Comparing the results, one can observe the difference in the potential core length between S1 and S2 simulations. The

Tabela 3: Potential core length and relative error of S1 and S2 simulations.

Simulation	$\delta_j^{95\%}$	Relative error
S1	5.57	40%
S2	6.84	26%
Mendez *et al.*	8.35	8%

results of the first case present a smaller $\delta_j^{95\%}$ when compared to results of S2 calculation, *i.e.*, 5,57 and 6.84, respectively. One can say that the solution of S1 computation is over dissipative when compared to the results of S2 study. The jet vanishes earlier in S1 simulation. The mesh which is used in the S1 test case is very coarse when compared with the grid used for S2 calculation. This lack of resolution can generate very dissipative solutions which yield the under prediction of the potential core length. The mesh refinement reduced in 14% the relative error of S2 computation when compared to the experimental data.

Profiles of $\langle U \rangle$ from S1 and S2 simulations, along the mainstream direction, and the evolution of $\langle U \rangle$ along the centerline and along the lipline are compared with numerical and experimental results in Fig. 4. The centerline and the lipline are indicated as (E) and (F) in Fig. 3. The dash-point line and the solid line stand for the results of the S1 and S2 test cases, respectively, in Fig. 4. The square symbols stand for the LES results of Mendez *et al.* (2010, 2012), while the triangular symbols stand for the experimental data of Bridges and Wernet (2008).

The comparison of profiles indicates that distributions of $\langle U \rangle$ calculated on S1 and S2 test cases correlates well with the references until $X = 5.0D$. The $\langle U \rangle$ profile calculated with S2 simulation at $X = 10.0D$ is under predicted when compared with the reference profiles. However, it is closer to the reference when compared with the results of S1 calculation. One can notice that $\langle U \rangle$ distributions along the centerline calculated by S1 and S2 computations correlates with the references in the regions which the grid presents a good resolution. When the mesh spacing increases, due to the mesh coarsening in the streamwise direction, the time average axial component of velocity start to correlate poorly with the reference. The time averaged axial component of velocity calculated by S1 simulation, along the lipline, correlates better with the reference than the same property calculated on S2 study. The second case overestimates the magnitude of $\langle U \rangle$ until $X \approx 6.0D$.

Figure 5 presents profiles of $\langle u^* v^* \rangle$ component of the Reynolds stress tensor. One can observe that the profiles achived in S1 and S2 simulations are really far from the numerical and experimental data. The solver has produced with succes the shape of $\langle u^* v^* \rangle$ profile. However, it fails to represent the peak of $\langle u^* v^* \rangle$ for all profiles compared.

The effects of the mesh on the SGS modeling are also studied in the present subsection. Figure 6 presents distributions of time averaged eddy viscosity, $\langle \mu_t \rangle$, calculated on S1 and S2. The Smagorinsky model (Smagorinsky, 1963; Lilly, 1965, 1967) is used on both simulations. This SGS closure is highly dependent on the local mesh size. One can notice that $\langle \mu_t \rangle$ presents higher values on the distributions obtained by S1. On the other hand, the eddy viscosity is only acting on the regions where the mesh is no longer very refined for the S2 study. The $\langle \mu_t \rangle$ is very low in the region where the grid spacing is small.

The eddy viscosity can contribute to the dissipative characteristic of the simulations. Specially for meshes with low point resolution. The divergence observed on the distribution of $\langle \mu_t \rangle$ calculated by S1 and S2 simulations is an example of such effect. However, it is important to notice that, even in regions where the mesh is not very refined, yet, not coarse, and where the eddy viscosity can be neglected, some distributions of properties, calculated by S2 test case, have shown to be very dissipative when compared with the LES reference and with the experimental data. Therefore, one can state that the truncation errors originated from the second order spatial discretization, used on the simulations here performed, can easily overcome the effects of SGS modeling if the grid spacing is not small enough. The issue is very important for the structured mesh approach. Increasing mesh resolution in the region of interest expressively rises up the number of points all over the computational domain. Local refinement for structured mesh is not straight forward and the code used in the current work does not have such approach available.

5.5 Subgrid Scale Modeling Study

After the mesh refinement study the three SGS models added to the solver are compared. S2, S3 and S4 simulations are performed using the static Smagorinsky model (Smagorinsky, 1963; Lilly, 1965, 1967), the dynamic Smagorinsky model (Germano, 1990; Moin *et al.*, 1991) and the Vreman model (Vreman, 2004), respectively. The same mesh with 50 million points is used for all three simulations. The configuration of the numerical studies is presented in Tab. 1. The same comparisons performed on the study of mesh refinement effects, Sec. 5.4, are performed for the SGS modeling study.

Effects of the SGS modeling on the time averaged results of the axial component of velocity are presented in the subsection. Table 4 presents the size of the potetial core of S2, S3 and S4 simulations and the numerical reference (Mendez *et al.*, 2010, 2012) along with the relative error compared with the experimental data (Bridges and Wernet, 2008).

Comparing the results, one cannot observe significant differences on the potential core length between S2, S3 and S4 test cases. The distribution of $\langle U \rangle$ calculated using the dynamic Smagorinky model has shown to be slightly more concentrated at the centerline region. S2 and S4 studies time averaged distribution of U are, on some small scale, more spread than the distribution obtained by S3 calculation.

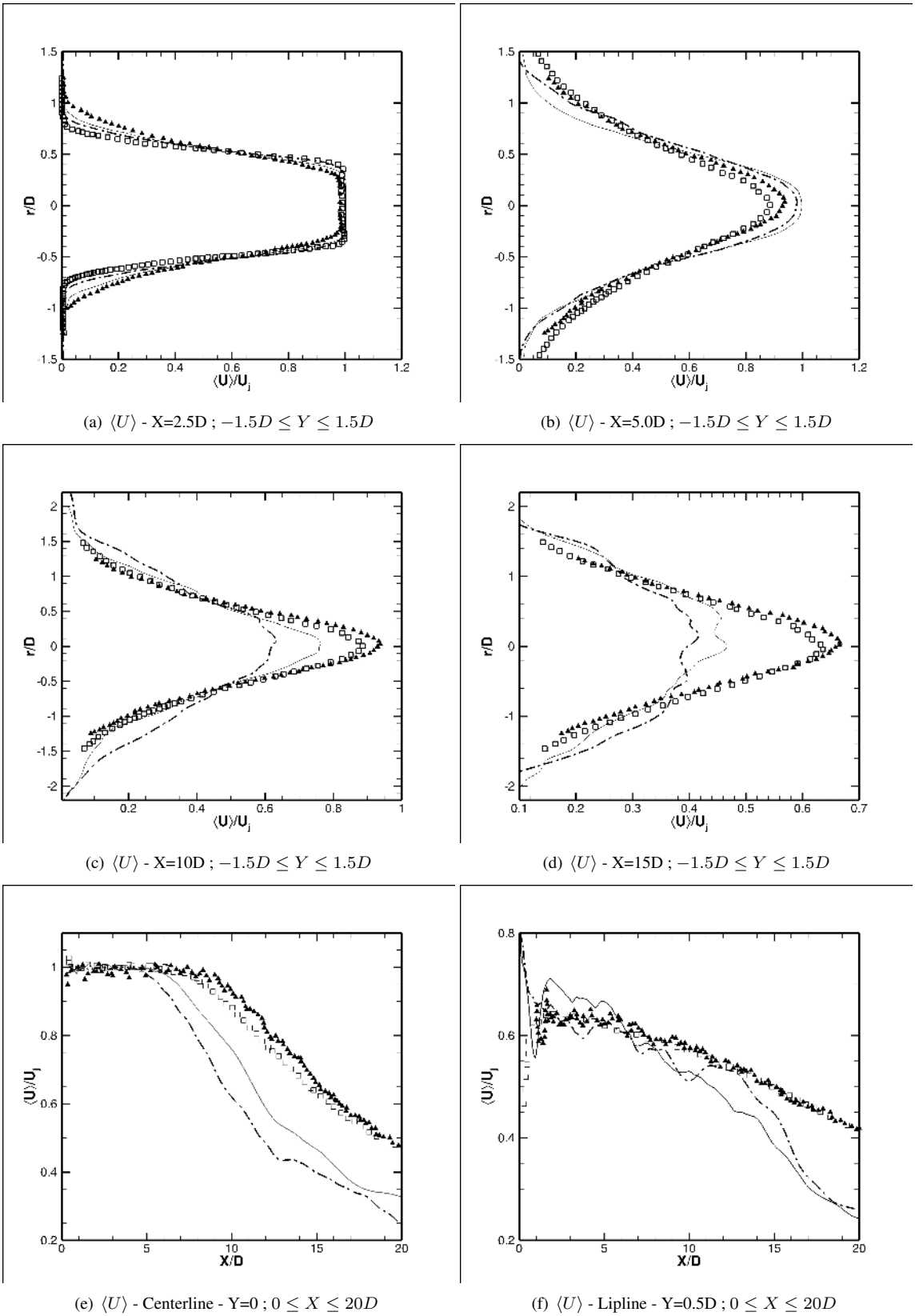

(a) $\langle U \rangle$ - X=2.5D ; $-1.5D \leq Y \leq 1.5D$

(b) $\langle U \rangle$ - X=5.0D ; $-1.5D \leq Y \leq 1.5D$

(c) $\langle U \rangle$ - X=10D ; $-1.5D \leq Y \leq 1.5D$

(d) $\langle U \rangle$ - X=15D ; $-1.5D \leq Y \leq 1.5D$

(e) $\langle U \rangle$ - Centerline - Y=0 ; $0 \leq X \leq 20D$

(f) $\langle U \rangle$ - Lipline - Y=0.5D ; $0 \leq X \leq 20D$

Figura 4: Profiles of averaged axial component of velocity at different positions within the computational domain. (▬•▬), S1 simulation; (▬), S2 simulation; (□), numerical data; (▲), experimental data.

Profiles of $\langle U \rangle$ from S2, S3 and S4 simulations, along the mainstream direction, and the evolution of $\langle U \rangle$ along the centerline and, also along the lipline, are compared with numerical and experimental results in Fig. 7. The solid line, the dashed line and the circular symbol stand for the profiles of $\langle U \rangle$ computed by S2, S3 and S4 test cases, respectively. The reference data are represented by the same symbols presented in the mesh refinement study.

The comparison of profiles indicates that distributions of $\langle U \rangle$ calculated on S2, S3 and S4 numerical studies correlates well with the references until $X = 5.0D$. For $X > 10.0D$ all SGS models fail to predict the correct profile. One can notice that the evolution of $\langle U \rangle$ along the centerline, calculated by all three simulations, are in good agreement with the

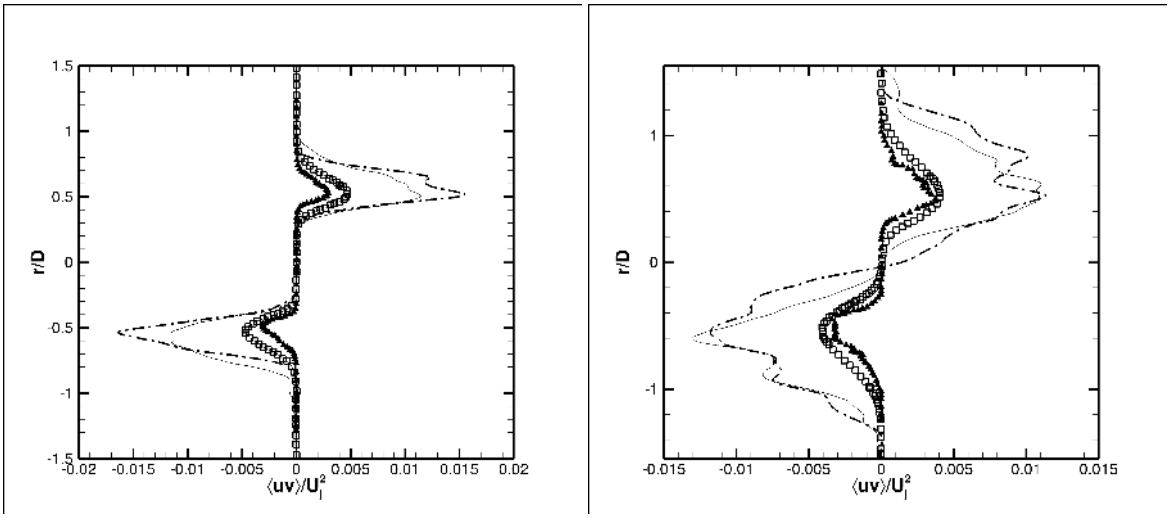

(a) $\langle u^* v^* \rangle$ - X=2.5D ; $-1.5D \leq Y \leq 1.5D$

(b) $\langle u^* v^* \rangle$ - X=5.0D ; $-1.5D \leq Y \leq 1.5D$

(c) $\langle u^* v^* \rangle$ - X=10D ; $-1.5D \leq Y \leq 1.5D$

(d) $\langle u^* v^* \rangle$ - X=15D ; $-1.5D \leq Y \leq 1.5D$

Figura 5: Profiles of the $\langle u^* v^* \rangle$ Reynolds shear stress tensor component, for S1 and S2 simulations, at different positions within the computational domain. (▬ • ▬), S1 simulation; (▬), S2 simulation; (□), numerical data; (△), experimental data.

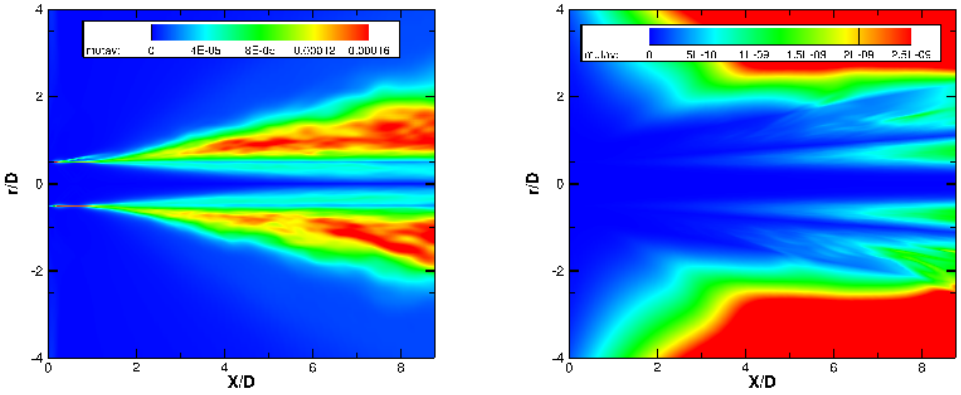

(a) Lateral view of $\langle \mu_t \rangle$ for S1 simulation.

(b) Lateral view of $\langle \mu_t \rangle$ for S2 simulation.

Figura 6: Lateral view and detailed view of time averaged eddy viscosity, $\langle \mu_t \rangle$, for S1 and S2 simulations.

numerical and experimental reference data at the region where the mesh presents a good resolution. Moreover, the three distributions calculated using different SGS closures have presented the very similar behavior. The dynamic Smagorinsky model and the Vreman model correlates better with the experimental data for $X < 5.0D$ than the classic Smagorinsky closure does. However, all simulations tend to not predict well the magnitude of $\langle U \rangle$ on the lipline when the mesh size increases, $X > 5.0D$.

Tabela 4: Potential core length and relative error of S2, S3 and S4 simulations.

Simulation	$\delta_j^{95\%}$	Relative error
S2	6.84	26%
S3	6.84	26%
S4	6.28	32%
Mendez *et al.*	8.35	8%

Figure 8 presents the profiles of $\langle u^* v^* \rangle$ component of the Reynolds stress tensor computed using three different SGS models, respectively. All numerical simulations performed in the present work have failed to correct predict the profiles of $\langle u^* v^* \rangle$ presented in Fig. 8. The peaks of the component of the Reynolds stress tensor does not correlate with the reference results. However, one should notice that the LES performed by the reference has also presented difficulties to calculate the same peaks. The cause of the issue could be related to an eventual lack of grid points in the radial direction. In spite of that, more studies on the subject are necessary in order to understand such behavior.

The distribution of the eddy viscosity, μ_t, is discussed in the current subsection. Figure 9 presents distributions of time averaged eddy viscosity calculated using different SGS models. All subgrid scale closures used in the present work, the static Smagorinsky (Smagorinsky, 1963; Lilly, 1965, 1967), the dynamic Smagorinsky (Germano *et al.*, 1991; Moin *et al.*, 1991) and the Vreman (Vreman, 2004) models, are dependent of the local mesh size by design. This characteristic is exposed on the lateral view of the flow presented in Fig. 9. The SGS models are only acting in the region where mesh presents a low resolution. Near the entrance domain, where the computational grid is very refined, the eddy viscosity can be neglected.

The remark goes in the same direction of the work of Li and Wang (2015), which indicates that SGS closures introduce numerical dissipation that can be used as a stabilizing mechanism. However, this numerical dissipation does not necessarily add more physics of the turbulence to the LES solution. Therefore, in the present work, the numerical truncation, which generates the dissipative characteristic of JAZzY solutions, have show to overcome the effects of the SGS modeling. The mesh need to be very fine in order to achieve good results with second order spatial discretizations. The grid refinement generates very small grid spacing. Consequently, the SGS models, which are strongly dependent on the filter width, does not affect much the solution. A LES of compressible flow configurations without the use of SGS closure would be welcome in order to complete such discussion.

6. CONCLUDING REMARKS

The current work is the study on effects of different subgrid scales models on perfectly expanded supersonic jet flow configurations using centered second-order spatial discretization. A formulation based on the the System I set of equations is used in the present work. The time integration is performed using a five-steps second order Runge-Kutta scheme. Four large eddy simulations of compressible jet flows are performed in the present research using two different mesh configurations an three different subgrid scale models. Their effects on the large eddy simulation solution are compared and discussed.

The mesh refinement study has indicated that in the region where the grid presents high resolution, the simulations are in good agreement with experimental and numerical references. For the mesh with 14 million points the simulation has produced good results for $X < 2.5D$ and $-1.5D < Y < 0.5D$. For the other mesh, with 50 million points, the simulations provided good agreement with the literature for $X < 5.0D$ and $-1.5D < Y < 0.5D$. The eddy viscosity, calculated by the static Smagorinsky model, presents very low levels in the region where the results have good correlation with the results of the literature.

The refined grid used on the mesh refinement study, mesh B, is used for the comparison of SGS models effects on the results of large eddy simulations. Three compressible jet flow simulations are performed using the classic Smagorinsky model (Smagorinsky, 1963; Lilly, 1965, 1967), the dynamic Smagorinsky model (Germano *et al.*, 1991; Moin *et al.*, 1991) and the Vreman model (Vreman, 2004). All three simulations presented similar behavior. Results presented good agreement with the reference for $X < 5.0D$. In the region where the grid is very fine and the results correlates well with the literature, the eddy viscosity, provided by the SGS model, is very low values. The reason is related to the fact that the SGS closures used in the current work are strongly dependent of the filter width, which is proportional to the local mesh size.

The numerical results indicated that it is possible to achieve good results using second-order spatial discretization. The mesh ought be well resolved in order to overcome the truncation errors from the low order numerical scheme. Very fine meshes originates very small filter width. Consequently, the effects of the eddy viscosity calculated by the SGS models on the solution become unimportant. The work of Li and Wang (2015) have presented similar conclusions for simplified problems. The authors indicate that SGS closures introduce numerical dissipation that can be used as a stabilizing mechanism. However, this numerical dissipation does not necessarily add more physics of the turbulence to the LES solution. Simulations without the use of any SGS model are welcome and could reinforce the argument.

The authors intent to present simulations using a more refined grid for the final version of the paper. The goal is to generate a mesh which uses the mesh B resolution of the refined region, for $X < 5.0$, all over the computational domain. The mesh will be used for other siulations using the three SGS closures tested in the present work. The resuls will be

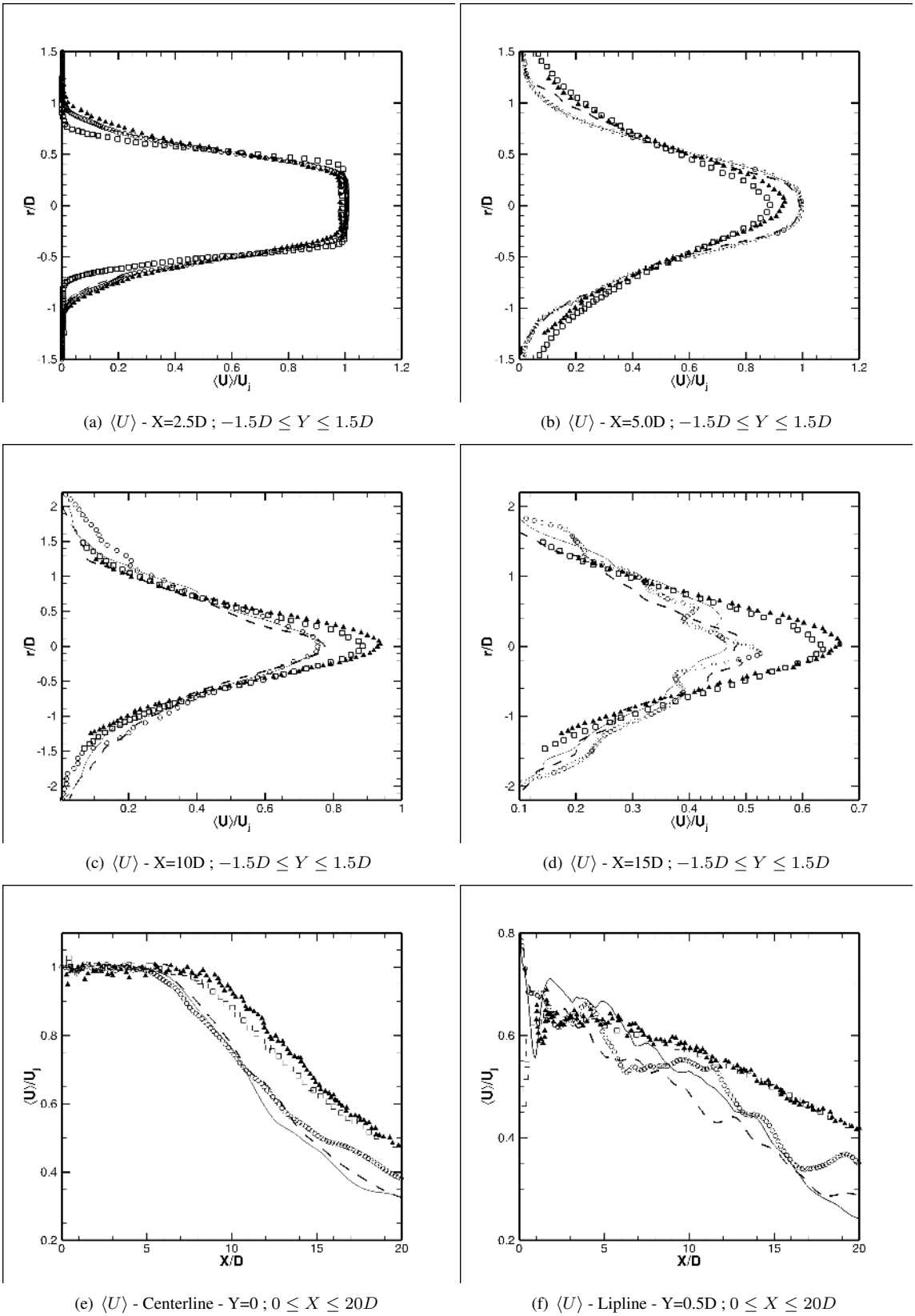

(a) $\langle U \rangle$ - X=2.5D ; $-1.5D \leq Y \leq 1.5D$

(b) $\langle U \rangle$ - X=5.0D ; $-1.5D \leq Y \leq 1.5D$

(c) $\langle U \rangle$ - X=10D ; $-1.5D \leq Y \leq 1.5D$

(d) $\langle U \rangle$ - X=15D ; $-1.5D \leq Y \leq 1.5D$

(e) $\langle U \rangle$ - Centerline - Y=0 ; $0 \leq X \leq 20D$

(f) $\langle U \rangle$ - Lipline - Y=0.5D ; $0 \leq X \leq 20D$

Figura 7: Profiles of averaged axial component of velocity at different positions within the computational domain. (━), S2 simulation; (▬ ▬), S3 simulation; (◯), S4 simulation; (□), numerical data; (▲), experimental data.

compared with the same S1, S2, S3 and S4 test cases and also with de reference data presented in this draft.

7. ACKNOWLEDGEMENTS

The authors gratefully acknowledge the partial support for this research provided by Conselho Nacional de Desenvolvimento Científico e Tecnológico, CNPq, under the Research Grants No. 309985/2013-7, No. 400844/2014-1 and No. 443839/2014-0. The authors are also indebted to the partial financial support received from Fundação de Amparo

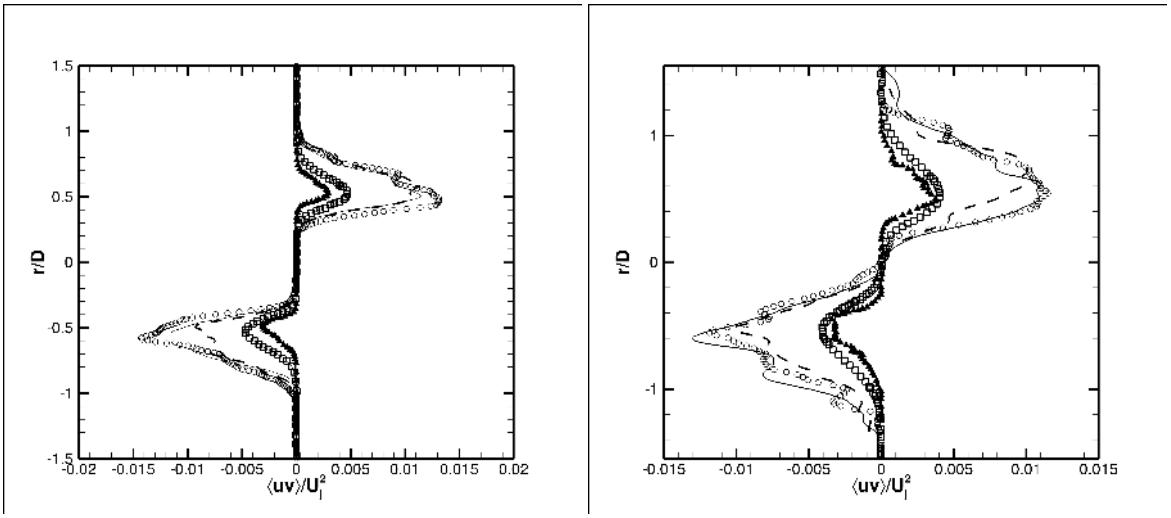

(a) $\langle u^* v^* \rangle$ - X=2.5D ; $-1.5D \leq Y \leq 1.5D$

(b) $\langle u^* v^* \rangle$ - X=5.0D ; $-1.5D \leq Y \leq 1.5D$

(c) $\langle u^* v^* \rangle$ - X=10D ; $-1.5D \leq Y \leq 1.5D$

(d) $\langle u^* v^* \rangle$ - X=15D ; $-1.5D \leq Y \leq 1.5D$

Figura 8: Profiles of the $\langle u^* v^* \rangle$ Reynolds shear stress tensor component, for S2, S3 and S4 simulations, at different positions within the computational domain. (━), S2 simulation; (▬), S3 simulation; (◯), S4 simulation; (□), numerical data; (▲), experimental data.

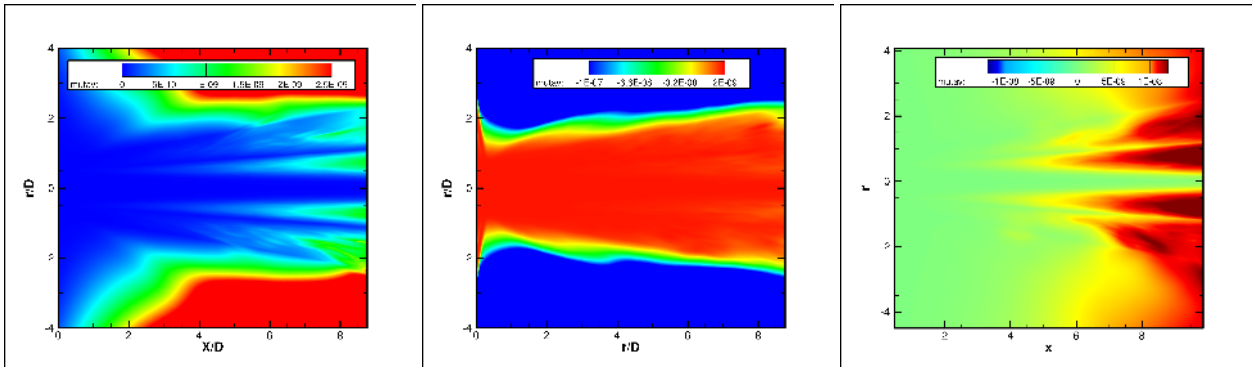

(a) $\langle \mu_t \rangle$ - S2 simulation.

(b) $\langle \mu_t \rangle$ - S3 simulation.

(c) $\langle \mu_t \rangle$ - S4 simulation.

Figura 9: Lateral view of time averaged eddy viscosity, $\langle \mu_t \rangle$, for S2, S3 and S4 simulations.

à Pesquisa do Estado de São Paulo, FAPESP, under the Research Grants No. 2008/57866-1, No. 2013/07375-0 and No. 2013/21535-0.

8. REFERENCES

ANSYS, 2016. "http://www.ansys.com/".

Bigarella, E.D.V., 2002. *Three-Dimensional Turbulent Flow Over Aerospace Configurations*. M.Sc. Thesis, Instituto Tecnológico de Aeronáutica, São José dos Campos, SP, Brasil.

Bodony, D. and Lele, S.K., 2005. "On using large-eddy simulation for the prediction of noise from cold and heated

turbulent jets". *Physics of Fluids*, Vol. 17, No. 8.
Bodony, D.J. and Lele, S.K., 2008. "Current status of jet noise predictions using large-eddy simulations". *AIAA Journal*, Vol. 46, No. 2, pp. 364–380.
Bogey, C. and Bailly, C., 2005. "Effects of inflow conditions and forcing on subsonic jet flows and noise". *AIAA Journal*, Vol. 43, No. 5, pp. 1000–1007.
Bogey, C., Marsden, O. and Bailly, C., 2012. "Influence of initial turbulence level on the flow and sound fields of a subsonic jet at a diameter-based reynolds number of 10^5". *Journal of Fluid Mechanics*, Vol. 701, pp. 352–385.
Brès, G., Nichols, J.W., Lele, S.K. and Ham, F.E., 2012. "Towards best pratices for jet noise predictions with unstructured large eddy simulations". In AIAA Paper No. 2012-2965*, Proceedings of the 42nd AIAA Fluid Dynamics Conference and Exhibit*. New Orleans, Louisiana, USA, p. 21.
Bridges, J. and Wernet, M.P., 2008. "Turbulence associated with broadband shock noise in hot jets". *AIAA paper*, Vol. 2834, p. 2008.
Germano, M., 1990. "Averaging invariance of the turbulent equations and similar subgrid scale modeling". In *Center for Turbulence Research Manuscript 116*. Stanford University and NASA - Ames Research Center.
Germano, M., Piomelli, U., Moin, P. and Cabot, W.H., 1991. "A dynamic subgridscale eddy viscosity model". *Physics of Fluids A: Fluid Dynamics*, Vol. 3, No. 7.
Jameson, A. and Mavriplis, D., 1986. "Finite volume solution of the two-dimensional euler equations on a regular triangular mesh". *AIAA Journal*, Vol. 24, No. 4, pp. 611–618.
Jameson, A., Schmidt, W. and Turkel, E., 1981. "Numerical solutions of the euler equations by finite volume methods using runge-kutta time-stepping schemes". In AIAA Paper 81–1259*, Proceedings of the AIAA 14th Fluid and Plasma Dynamic Conference*. Palo Alto, Californa, USA.
Junqueira-Junior, C.A., Yamouni, S., Azevedo, J.L.F. and Wolf, W.R., 2015. "Large Eddy Simulations of Supersonic Jet Flows for Aerocoustic Applications". In AIAA paper 2015-3306*, Proceedings of 33rd AIAA Applied Aerodynamics Conference*. Dallas, TX, USA.
Junqueira-Junior, C.A., 2016. *Development of a Parallel Solver for Large Eddy Simulation of Supersonic Jet Flow*. Ph.D. thesis, Instituto Tecnoógico de Aeronáutica, São José dos Campos, SP, Brazil.
Lele, S.K., 1992. "Compact finite difference schemes with spectral-like resolution". *Journal of Computatinoal Physics*, Vol. 103, pp. 16–42.
Lele, S.K., Mendez, S., Ryu, J., Nichols, J., Shoeybi, M. and Moin, P., 2010. "Large-eddy simulation: Achievements and challenges". *Procedia Engineering*, Vol. 6, No. 4, pp. 84–93.
Li, Y. and Wang, Z.J., 2015. "A priori and a posteriori evaluation of subgrid stress models with the burger´s equation". In AIAA-2015-1283*, Proceedings of 53rd AIAA Aerospace Sciences Meeting*. Kissimmee, Florida, U.S.A, p. 20.
Lilly, D.K., 1967. "The representation of small-scale turbulence in numerical simulation experiments". In IBM Form No. 320-1951*, Proceedings of the IBM Scientific Computing Symposium on Environmental Sciences*. Yorktown Heights, N.Y., pp. 195–210.
Lilly, D.K., 1965. "On the computational stability of numerical solutions of time- dependent non-linear geophysical fluid dynamics problems". *Monthly Weather Review*, Vol. 93, No. 1, pp. 11–25.
Mahesh, K., Constantinescu, G. and Moin, P., 2004. "A numerical method for large-eddy in complex geometries simulation". *Journal of Computatinoal Physics*, Vol. 197, pp. 215–240.
Mendez, S., Shoeybi, M., Sharma, A., Ham, F.E., Lele, S.K. and Moin, P., 2010. "Large-eddy simulations of perfectly-expanded supersonic jets: Quality assessment and validation". In AIAA Paper No. 2010–0271.
Mendez, S., Shoeybi, M., Sharma, A., Ham, F.E. and Moin, S.K.L.P., 2012. "Large-eddy simulations of perfectly-expanded supersonic jets using an unstructured solver". *AIAA Journal*, Vol. 50, No. 5, pp. 1103–1118.
Moin, P., Squires, K., Cabot, W. and Lee, S., 1991. "A dynamic subgrid-scale model for compressible turbulence and scalar transport". *Physics of Fluids A: Fluid Dynamics (1989-1993)*, Vol. 3, No. 11, pp. 2746–2757.
Sagaut, P., 2002. *Large Eddy Simulation for Incompressible Flows*. Springer.
Smagorinsky, J., 1963. "General circulation experiments with the primitive equations: I. the basic experiment". *Monthly Weather Review*, Vol. 91, No. 3, pp. 99–164.
Speziale, C.G., Erlebacher, G., Zang, T.A. and Hussaini, M.Y., 1988. "The subgrid-scale modeling of compressible turbulence". *Physics of Fluids (1958-1988)*, Vol. 31, No. 4, pp. 940–942.
Turkel, E. and Vatsa, V.N., 1994. "Effect of Artificial Viscosity on Three-Dimensional Flow Solutions". *AIAA Journal*, Vol. 32, No. 1, pp. 39–45.
Vreman, A.W., 2004. "An eddy-viscosity subgrid-scale model for turbulent shear flow: Algebraic theory and applications". *Physics of Fluids*, Vol. 16, No. 10.
Vreman, A.W., 1995. *Direct and Large-Eddy Simulation of the Comperssible Turbulent Mixing Layer*. Ph.D. thesis, Universiteit Twente.
Wolf, W. and Lele, S.K., 2011. *Airfoil Aeroacoustics: LES and Acoustic Analogy Predictions*. Ph.D. thesis, Stanford, Stanford, CA, USA.

9. RESPONSIBILITY NOTICE

The authors are the only responsible for the printed material included in this paper.